Integrating Materials and Manufacturing Innovation
https://doi.org/10.1007/s40192-025-00425-2

TECHNICAL ARTICLE

Efficient Calibration Strategy for Crystal Plasticity Constitutive Law to Model Additively Manufactured Alloys

Sourav Saha[1] · Jiachen Guo[2] · Chanwook Park[3] · Reza Batley[1] · Wing Kam Liu[2,3,4]

Received: 17 July 2025 / Accepted: 23 September 2025

Abstract

Spatial heterogeneity in microstructure presents a significant challenge for part qualification in metal additive manufacturing, particularly when relying on physically accurate computational models to replace costly trial-and-error testing. Reliable structural simulation needs a large amount of offline data and several very expensive forward runs to learn the most appropriate material model parameters. This work introduces a systematic framework for accurately calibrating crystal plasticity (CP) material law parameters using limited characterization data. The calibrated CP law is validated through blind predictions of mechanical responses in laser powder-bed fusion Inconel 625 (IN 625) tensile coupons across varying build orientations and strategies. Two surrogate modeling approaches—a higher-order proper generalized decomposition (HOPGD) and a novel interpolating neural network (INN)—are evaluated for their ability to approximate full-field simulations. The study presents an adaptive sampling strategy to efficiently utilize an offline database and outlines a methodology for representing microstructure from sparse characterization inputs. Results demonstrate that the differentiable INN surrogate achieves accurate calibration with significantly reduced data requirements and avoids reliance on computationally expensive genetic algorithms. Both surrogate models exhibit strong predictive performance, and the proposed workflow was instrumental in winning the 2022 NIST Additive Manufacturing Benchmark Challenge.

Keywords Additive manufacturing · Reduced-order model · Crystal plasticity · Build orientation · Interpolating neural network · Proper generalized decomposition

Introduction

Three-dimensional printing of metallic alloys has revolutionized the manufacturing science landscape [1–3]. Laser powder-bed fusion (LPBF) is a major class of metal 3D printing technology [4]. In LPBF, consecutive layers of metal powders are spread, and each layer is melted with a laser beam that traces the geometry of a specific part. After each layer of powder is melted, a new layer is re-coated, and the process repeats until the part is finished. The continuous melting, solidification, and remelting of metal powders give rise to complex non-equilibrium multiphysics and multiscale physical phenomena [5–8]. As a consequence, the microstructure exhibits unique features after solidification [9–11]. An important feature is the directional solidification of LPBF alloys [12, 13]. This imparts variation of mechanical properties with respect to the build direction [14–16]. The nature of this variation with build direction is, in turn, dependent on the process parameters such as scan speed, laser power, hatch spacing, and scan strategy [17–19]. This opens up a large materials design and optimization landscape. However, this also means that the design of LPBF metal alloy is a high-dimensional problem with numerous sources of uncertainty. Therefore, the Edisonian trial-and-error approach to finding the most suitable design space for LPBF is prohibitive.

Computational methods to analyze, design, and quantify uncertainties in the LPBF process have become very popular. Several studies proposed a process–structure–property

✉ Sourav Saha
souravsaha@vt.edu

[1] Kevin T. Crofton Department of Aerospace and Ocean Engineering, Virginia Polytechnic Institute and State University, Blacksburg, VA 24060, USA

[2] Theoretical and Applied Mechanics, Northwestern University, Evanston, IL 60208, USA

[3] Department of Mechanical Engineering, Northwestern University, Evanston, IL 60208, USA

[4] Co-founder, HIDENN-AI, LLC, Oak Brook, IL 60253, USA

Published online: 11 October 2025

linkage via computational methods [20, 21]. These *linkage* studies resort to a wide array of methods, including computational fluid dynamics (CFD) [22–24], finite element method (FEM) [25, 26], cellular automata (CA) [27, 28], kinetic Monte Carlo (kMC) [29], and crystal plasticity finite element or Fast Fourier Transform (FFT) methods [30, 31]. However, all of these computational methods are relatively expensive when performed at the spatiotemporal resolution of experiments. This poses two challenges: a) calibrating the physical parameters of the models becomes extremely time-consuming ([31] shows 3.6 h of calibration time with a genetic algorithm), and b) a real-time prediction of the system response is extremely difficult to obtain. This article aims to establish a connection between microstructure and properties. Thus, this discussion will focus on the challenges in calibrating models based on microstructure, as well as the solutions suggested in this article to explore innovative calibrating strategies to model the directional dependence of the mechanical properties in LPBF IN 625 alloys.

Material laws based on crystal plasticity (CP) are widely utilized to define the microstructure–property relationship in multiscale simulations based on continuum mechanics [32, 33]. What makes this material law distinctive is its ability to model plastic slip deformations and dislocation interactions at the crystallographic level within a continuum setting. However, CP material laws usually have multiple parameters to be calibrated [30, 34]. These parameters are calibrated by an experiment (usually a limited number of uniaxial tensile/compressive tests) [35, 36]. The calibration requires matching the model response with experimental results by varying the model parameters. The process demands numerous time-consuming forward simulations. The usual trend is to use a surrogate model to replace the expensive forward simulation [37, 38]. Different surrogate models are proposed, including higher-order proper generalized decomposition [30], artificial neural network [39], Gaussian process regression [37], reinforcement learning method [40], and curve fitting [41]. Modelers also need to select an optimization algorithm alongside the surrogate, such as a genetic algorithm [35, 42] or a gradient-based method [31]. This process of calibration faces two challenges: a) without a proper sampling strategy, the amount of data required to develop the surrogate can be huge, and b) the use of gradient-free optimization is extremely time-consuming. Consequently, it is essential to develop a method that a) demands considerably less sampling data, and b) is differentiable, thereby allowing for the application of gradient-based optimization techniques. The present work addresses this gap by demonstrating a novel adaptive sampling strategy along with data-driven, efficient, and differentiable surrogate model.

An overview of the work presented in this article is shown in Fig. 1. The article discusses how to use the microstructure characterization and mechanical testing data systematically, produce representative microstructure, apply innovative calibration strategies suitable for sparse datasets, and determine the mechanical response for unseen cases. Due to the uncertainty in the manufacturing dataset, the National Institute of Standards and Testing (NIST) Additive Manufacturing Benchmark Challenge 2022 dataset is used for calibration and benchmarking the solution. The current work proposes two different surrogate models for calibrating the material law: (a) higher-order proper generalized decomposition (HOPGD) [43, 44] and (b) a novel deep learning method called interpolating neural network (INN) [45] combined

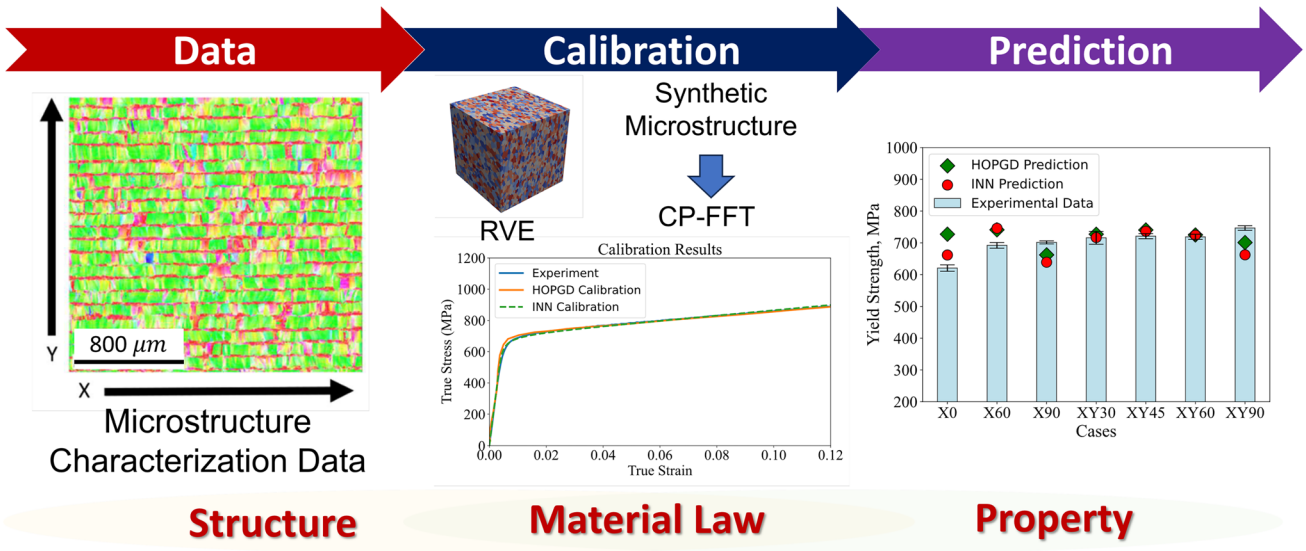

Fig. 1 Overview of the data-calibration-prediction workflow presented in the article

with an adaptive sampling strategy for calibrating the CP material law parameters. Using the calibrated CP parameters, an FFT-based solver [46] is applied to predict the mechanical properties of IN 625 built with two different scan strategies and along different orientations compared to the build direction. This article is organized as follows: Sect. Benchmark Data from NIST AM Bench 2022 briefly discusses the experimental calibration data. Computational Method section goes into the details of the computational aspects of the study. Results section presents a comparative discussion between INN and HOPGD and the effects of scanning strategy and build direction on the mechanical response of IN 625 coupon.

Benchmark Data from NIST AM Bench 2022

Benchmark experimental data for this work are taken from the National Institute of Standards and Technology (NIST) Additive Manufacturing Benchmark Challenge 2022. A comprehensive discussion on the challenge is provided in [47]. The article limits the discussion to highlight the important points only. The goal of providing a very limited set of experimental data is to ensure that the calibrated computational models work in unforeseen scenarios.

Inconel 625 is used as the manufacturing material. Moser et al. [47] provided more details on the powder composition of IN 625. The parts are built on $252mm \times 252mm$ 1045 steel alloy build-plate with low velocity N_2 cover gas. No post-build heat treatment is applied. The manufacturing parameters are: infill laser power 195 Watt, infill scanning speed 800 mm/s, contour laser power 100 W, contour scanning speed 900 mm/s, layer thickness 20 μm, and hatch spacing 100 μm. Two different scanning strategies are used to build parts as shown in Fig. 2a. The *XY-scan strategy* implies that the laser is alternately scanned in the X and Y directions (perpendicular to each other) for subsequent build layers. The *X-scan strategy* implies that the laser only travels back and forth along the X direction. Mini tensile specimens are cut from the manufactured blocks (dimensions are shown in Fig. 2b) using wire electrical discharge machining (EDM). The orientations of the mini tensile specimens are $0^0, 30^0, 45^0, 60^0$, and 90^0 with respect to the build direction. Four such specimens are cut from each block for each material condition, and there are three blocks in total per condition. The dimensions of the tensile coupons are according to ASTM E8 standard and are presented in Fig. 3.

The microstructure characterization information, such as Electron Backscatter Imaging (EBSD), X-ray computed tomography, and high-energy X-ray diffraction, is provided in the dataset. However, for this work, only EBSD characterization data are used. Figure 4 exhibits a sample of the EBSD tile provided by NIST. EBSD is performed on three orthogonal planes from a block manufactured by each scan strategy. More details on the EBSD acquisition parameters can be found in [47]. However, the X-scan strategy shows strong 101 pole alignment with the build direction, whereas the XY-scan strategy shows a mix between 001 and 101 poles.

Tensile testing experiments are conducted at room temperature. A nominal strain rate of $0.001s^{-1}$ is applied until failure on an MTS 858 Mini Bionix II servo-hydraulic load

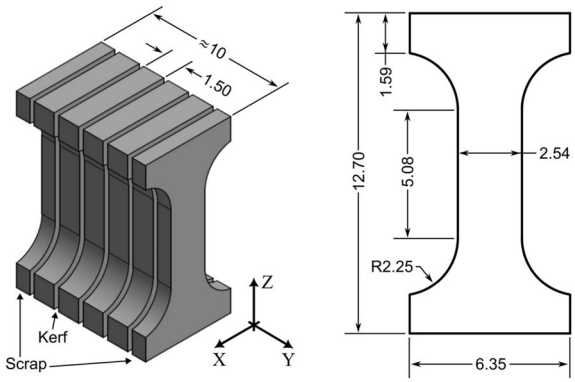

Fig. 3 Dimensions (in mm) of the mini tensile coupons used for prediction. Adopted from [47]

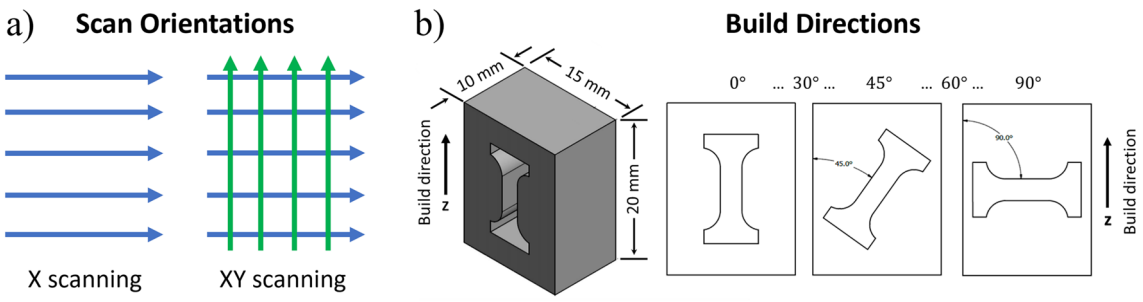

Fig. 2 **a** X and XY scanning strategies for building IN 625 samples. **b** Different orientations of the mini tensile coupon cut from the build [47]. 0^0 means the tensile axis is along the build direction

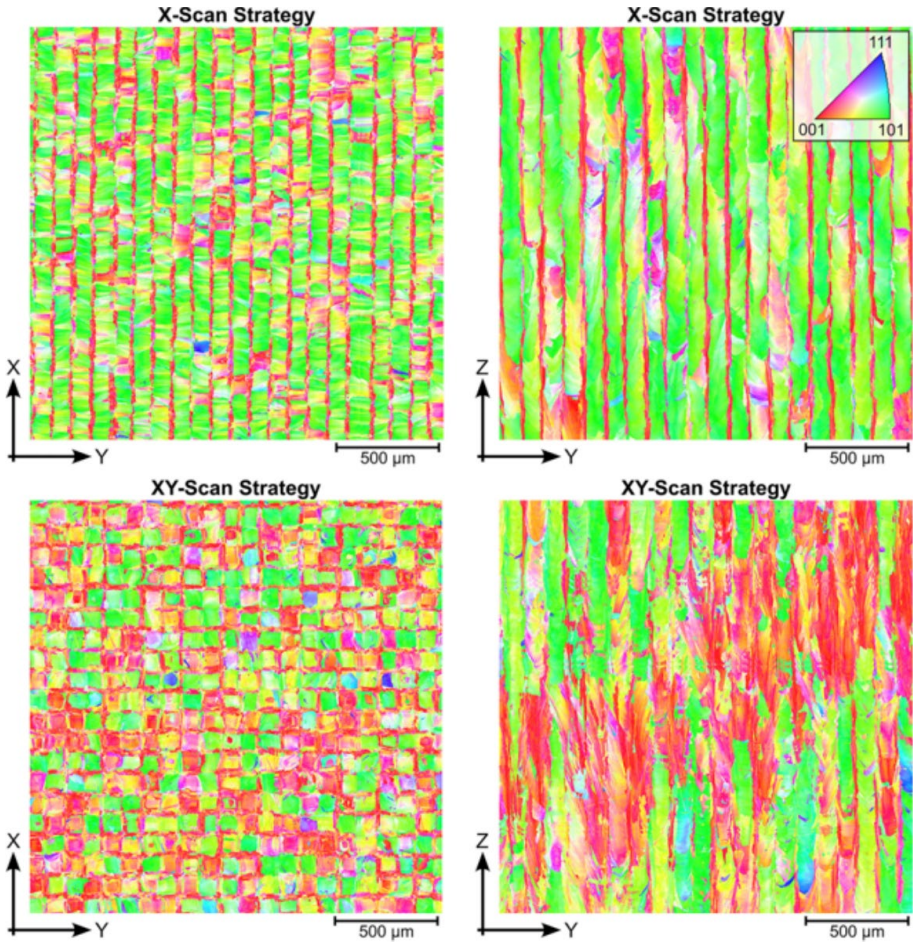

Fig. 4 Electron Backscatter Diffraction (EBSD) characterization for X and XY scanning strategies [47]. Build direction is the reference direction for the IPF

frame under displacement control. Prior to mechanical testing, all measurement devices were calibrated to ensure accuracy. The linear variable differential transformer (LVDT) and a load cell rated for 25 kN were calibrated, with the calibration report indicating a maximum error of 0.32% in tensile measurements within the operational range of 0%–60% of the load cell capacity. The extensometer used for displacement measurements was calibrated using an Epsilon Model 3590VHR Displacement Calibrator. This procedure verified measurement accuracy across the full extension range, with a maximum error remaining below 1% [47].

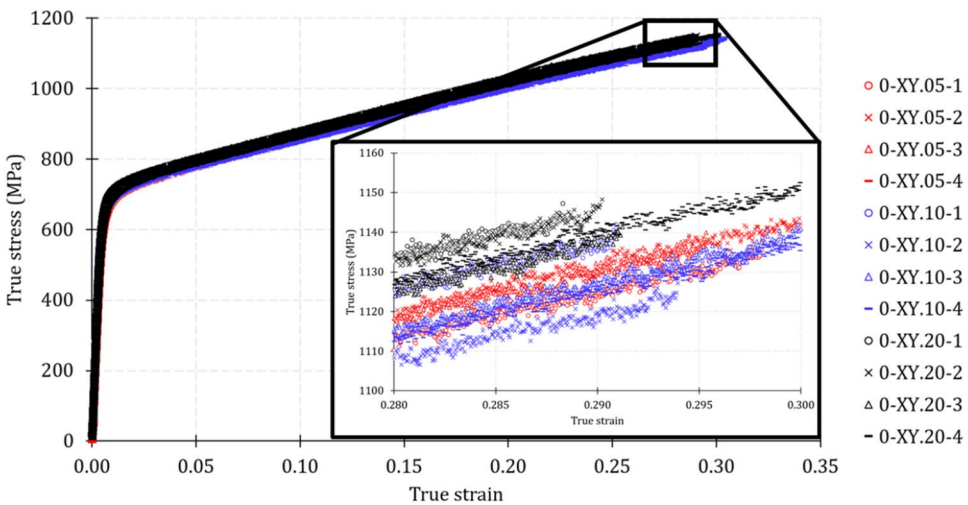

Fig. 5 Uniaxial tensile test data for calibration (XY-scan strategy and loading along the build orientation). "A-XY.B-C" stands for A degree tensile orientation, XY-scan strategy, B block number, and C specimen number [47]

A set of 12 uniaxial tensile test experiments are provided for calibration. Figure 5 shows the true strain vs true stress curves for the calibration case with XY-scan strategy and 0^0 orientation. The mean of this set of stress–strain data is used as the target for calibration.

Computational Method

This section will first discuss the steps required to generate representative microstructures from characterization data and the strategies to model the directional nature of the grains with respect to the loading direction. The discussion continues to elaborate on the CP material law and parameters that need to be calibrated. Calibration methodology, including a brief introduction to HOPGD and INN, is added at the end.

Microstructure Generation

Statistical features extracted from EBSD analysis are used to reconstruct a representative microstructure. The voxel-based microstructure is generated using the DREAM3D software suite [48]. To ensure physical fidelity, the reconstructed microstructure satisfies several key constraints: (1) It reflects the mixed elongated and equiaxed grain morphology typical of LPBF structures, (2) the voxel resolution is sufficient to capture the smallest grains, (3) the domain size is large enough to represent bulk mechanical behavior, and (4) the crystallographic texture is accurately incorporated.

The NIST Additive Manufacturing Benchmark Dataset provides EBSD data for both X- and XY-scan strategies on the XY and YZ planes. Since loading is applied along the Z-direction, statistical features from the YZ plane are primarily used, while the XY-scan data inform the grain aspect ratio. Key statistical descriptors used in reconstruction are shown in Fig. 6. Grain size statistics, including maximum and minimum equivalent spherical diameters, are used to match a log-normal distribution in DREAM3D, ensuring consistency with experimental averages. Grain elongation is incorporated via aspect ratio, and texture information is directly imported from.ang files.

To model the effect of build orientation, a large representative cube is first generated. Smaller sub-volumes are then extracted at specific angles (e.g., 30°, 45°, 60°, and 90°) to simulate different orientations. Figure 7a and b illustrates a sample reconstructed microstructure. Figure 7a shows grains colored by IPF on two orthogonal planes for the X-scan specimen. It is apparent from the figure that the reconstructed microstructure is able to capture the elongated grains in the structure. Note that the reconstructed microstructure is a scaled-down version of the EBSD representation. Hence, the grains are more pronounced. Figure 7b presents an example of RVE used in this work for 30° rotated sample from the X-scan build. The RVE is a 1000μm cube. A closer look reveals that the grains are extended at an angle, capturing the effect of build orientation.

Each voxel represents 5 μm physical dimension. Numerical tests confirm that a cube with 1000 μm sides is sufficient to capture microstructural variability. Depending on orientation, the final microstructures contain between 770 and 1131 grains.

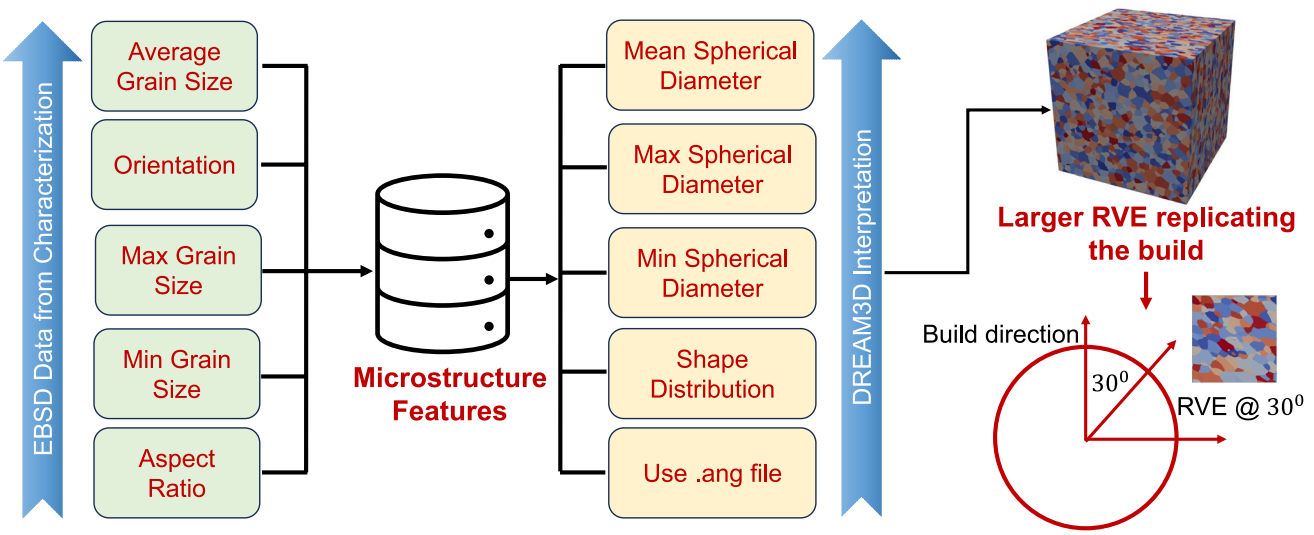

Fig. 6 Microstructural features considered to generate the representative structure with build direction

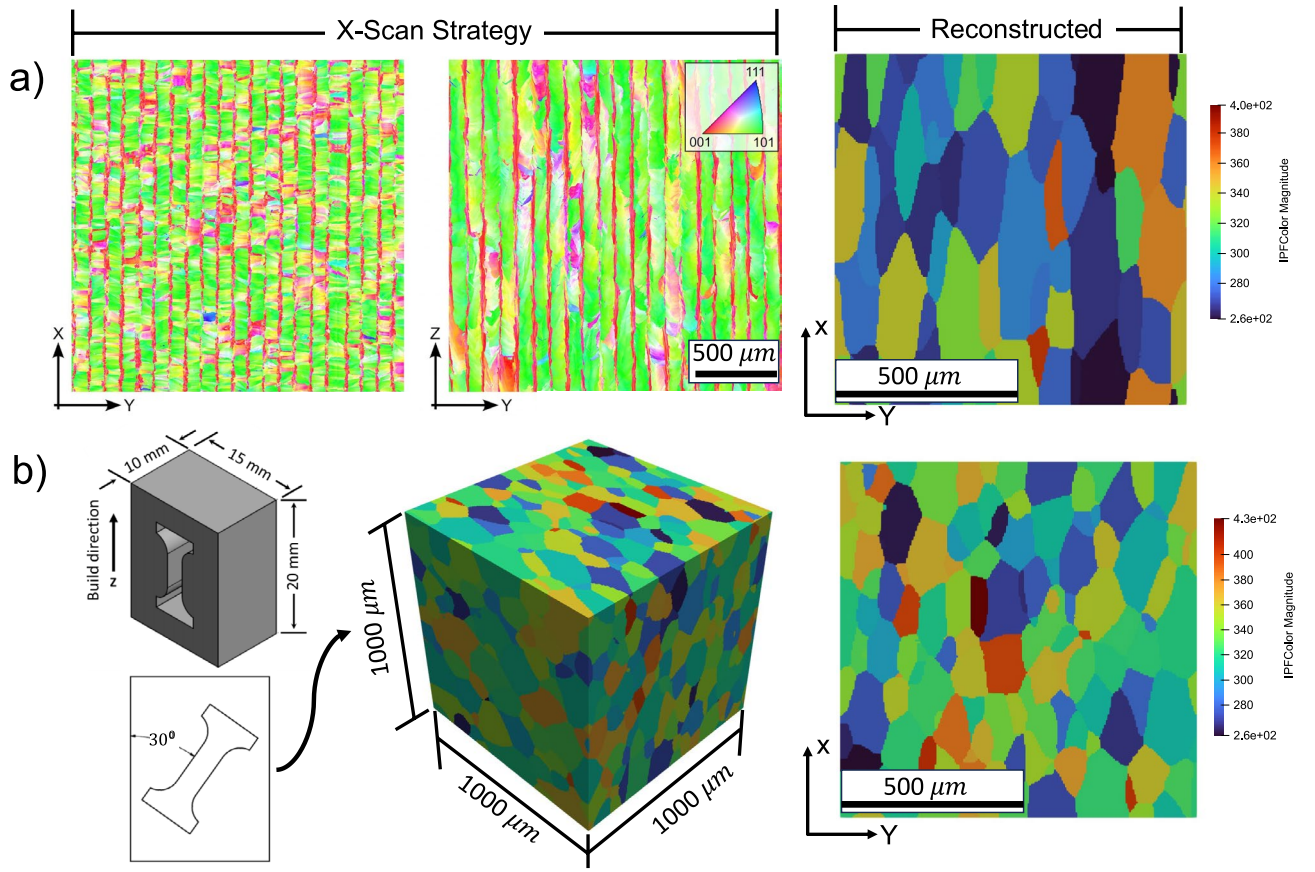

Fig. 7 **a** Comparison between the reconstructed microstructure of X-scanned and build-oriented specimen, and EBSD result, and **b** representative volume element of a 30-degree oriented sample

Material Law and Calibration Process

Crystal plasticity material law uses local deformation gradient, $\boldsymbol{F}$, which is multiplicatively decomposed, and the individual contributions are written as,

$$\boldsymbol{F} = \boldsymbol{F}^{e} \cdot \boldsymbol{F}^{in} \tag{1}$$

$\boldsymbol{F}^{e}$ and $\boldsymbol{F}^{in}$ are the elastic and inelastic parts of the deformation gradient, respectively. The deformation gradient is related to the elastic material law by

$$\boldsymbol{S}^{e} = \boldsymbol{C}^{SE} : \boldsymbol{E}^{e} = \frac{1}{2}\boldsymbol{C}^{SE} : \left[(\boldsymbol{F}^{e})^{T} \cdot \boldsymbol{F}^{e} - \boldsymbol{I}_{2}\right], \tag{2}$$

where $\boldsymbol{E}^{e}$ is the elastic Green–Lagrange strain, $\boldsymbol{S}^{e}$ is the second Piola–Kirchhoff stress, $\boldsymbol{C}^{SE}$ is the fourth-order elastic stiffness tensor, and $\boldsymbol{I}_{2}$ is the second-order identity tensor. In this article, $\boldsymbol{F}^{in} = \boldsymbol{F}^{p}$ is assumed where $\boldsymbol{F}^{p}$ is the plastic part of the deformation gradient. The plastic deformation gradient can be written in terms of the plastic velocity gradient by $\boldsymbol{L}^{p} = \dot{\boldsymbol{F}}^{p} \cdot (\boldsymbol{F}^{p})^{-1}$. The plastic shear rate $\dot{\gamma}^{\alpha}$ in slip system α is given by,

$$\boldsymbol{L}^{(p)} = \sum_{\alpha=1}^{N_{slip}} \dot{\gamma}^{(\alpha)} \left(\boldsymbol{s}_{0}^{(\alpha)} \otimes \boldsymbol{n}_{0}^{(\alpha)}\right). \tag{3}$$

Here $\boldsymbol{s}_{0}^{(\alpha)}$ and $\boldsymbol{n}_{0}^{(\alpha)}$ are the unit vectors defining the slip direction and slip plane normal for slip system α in the undeformed configuration. N_{slip} is the number of active slip systems (active slip systems for FCC system can be found in [49]), and $\otimes$ is the dyadic product. The resolved shear stress, $\tau^{(\alpha)}$ on the slip plane is written in terms of the plastic shear rate $\dot{\gamma}^{(\alpha)}$. The resolved shear stress is given by,

$$\tau^{(\alpha)} = \boldsymbol{\sigma} : \left(\boldsymbol{s}^{(\alpha)} \otimes \boldsymbol{n}^{(\alpha)}\right) \tag{4}$$

$\boldsymbol{\sigma}$ is the Cauchy stress, $\boldsymbol{s}$ is the slip direction, and $\boldsymbol{n}$ is the slip normal.

$$\boldsymbol{\sigma} = \frac{1}{J_{e}}\left[\boldsymbol{F}^{e} \cdot \boldsymbol{S}^{e} \cdot (\boldsymbol{F}^{e})^{T}\right] \tag{5}$$

$$\boldsymbol{s}^{(\alpha)} = \boldsymbol{F}^{e} \cdot \boldsymbol{s}_{0}^{(\alpha)} \tag{6}$$

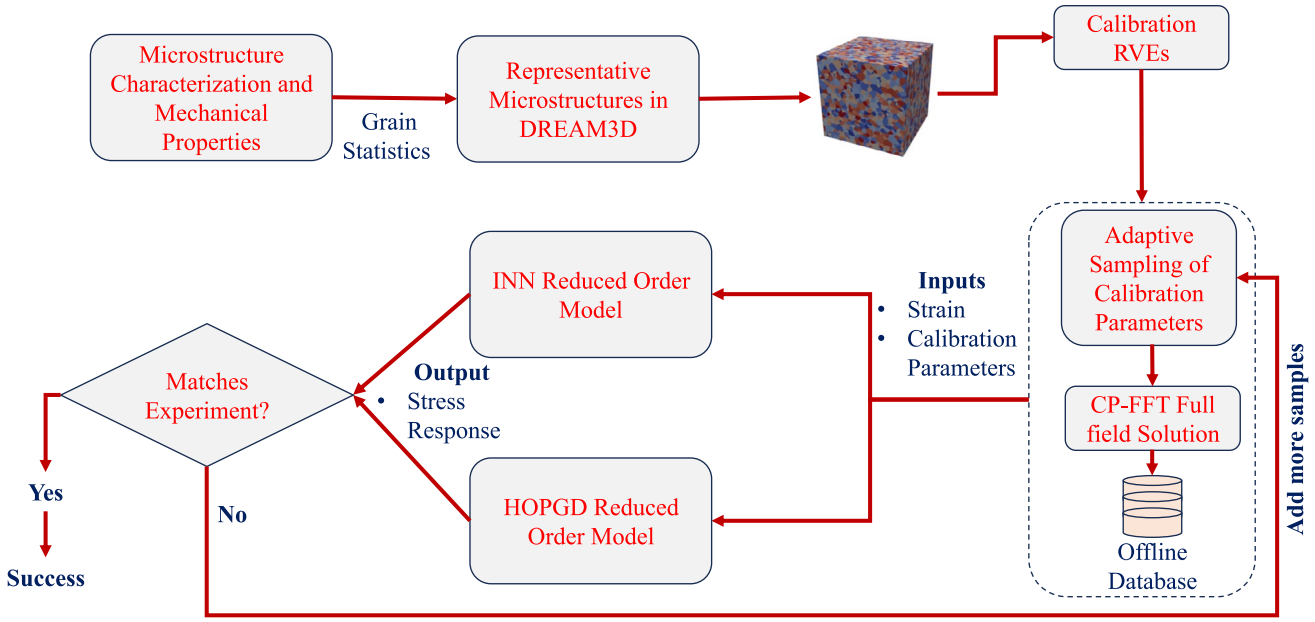

Fig. 8 Flowchart showing the calibration procedure

$$\boldsymbol{n}^{(\alpha)} = \boldsymbol{n}_0^{(\alpha)} \cdot (\boldsymbol{F}^e)^{-1}. \tag{7}$$

J_e is the determinant of $\boldsymbol{F}^e$. The hardening term $\dot{\gamma}^{(\alpha)}$ is updated by

$$\dot{\gamma}^{(\alpha)} = \dot{\gamma}_0 \left| \frac{\tau^{(\alpha)} - a^{(\alpha)}}{\tau_0^{(\alpha)}} \right|^{(m-1)} \operatorname{sgn}\left(\frac{\tau^{(\alpha)} - a^{(\alpha)}}{\tau_0^{(\alpha)}} \right). \tag{8}$$

Here $\dot{\gamma}_0$ is a reference shear rate, and m is the exponent related to material strain rate sensitivity. The deformation resistance shear stress τ_0 and back stress $a^{(\alpha)}$ are expressed as

$$\dot{\tau}^{(\alpha)} = H \sum_{\beta=1}^{N_{slip}} q^{\alpha\beta} \left| \dot{\gamma}^{(\beta)} \right| - R\tau^{(\alpha)} \sum_{\beta=1}^{N_{slip}} \left| \dot{\gamma}^{(\beta)} \right|, \tag{9}$$

$$\dot{a}^{(\alpha)} = h\dot{\gamma}^{(\alpha)} - ra\left| \dot{\gamma}^{(\alpha)} \right|, \tag{10}$$

where β is a slip system, H and h are direct hardening coefficients, R and r are the dynamic recovery constants, and $q^{\alpha\beta}$ is the latent hardening ratio. $q^{\alpha\beta}$ is given by

$$q^{\alpha\beta} = \kappa + (1 - \kappa)\delta^{\alpha\beta}. \tag{11}$$

Here κ is a latent hardening parameter. To solve the equilibrium equations with the CP material law, this work uses an in-house FFT solver. More details on the algorithm followed in this article are provided in [46] and [50]. Furthermore, the exact implementation of the solver by the authors on similar problems is found in [30].

Table 1 A summary of crystal plasticity parameters

Material property	Significance
C1111	Elastic constant
C1122	Elastic constant
C2323	Elastic constant
$\dot{\gamma}_0$	Reference shear rate
m	Hardening exponent
τ_0	Resolved shear stress at yield
a_0	Initial back stress
H,h	Hardening factor
R,r	Recovery factor

A summary of the CP parameters used in this work, and their physical significance is in Table 1. In the current work, $\dot{\gamma}_0$, τ_0, m, H, h, and κ (which is an internal variable (see Table 1)) are calibrated. Other parameters are either taken from [51] or literature. The parameters are chosen: a) to faithfully capture hardening for uniaxial loading and b) using heuristics and experience from previous work to reduce data generation by excluding less important parameters. As suggested in Table 1, $\dot{\gamma}_0$, τ_0, H, h, and m will control the hardening and yield behavior. κ is chosen to faithfully model the back-stress evolution in the case of repeated loading. However, this last term is not mandatory to calibrate for the problem solved in this article and could have been excluded. Moreover, R and r are not considered as these parameters become more important for cyclic loading. Determining these six parameters poses

an optimization problem to match the computed tensile response with the experiment by varying the simulation parameters. If the calibration parameters are expressed as $\boldsymbol{p} = \{\dot{\gamma}_0, \tau_0, m, H, h, \kappa\}$, the true stress along loading direction σ, and the true strain is ϵ, the optimization problem looks like,

$$\boldsymbol{p}^* = \arg\min_{\boldsymbol{p}} J\left(\sigma^{computed}(\epsilon, \boldsymbol{p}), \sigma^{experiment}(\epsilon)\right). \tag{12}$$

Here J is the objective function. For this work, J is the mean squared error between the experimental and computational stress values.

An overview of the calibration steps is shown in Fig. 8. EBSD statistics are used to generate a representative volume element (RVE) for calibration. EBSD data from the XY-scan strategy are used to generate the RVE. The RVE for calibration is not of the same size as the RVE for prediction. A cubic RVE of dimension $750\mu m$ is used for calibration. The calibration sample had 321 grains. The size is determined by increasing the RVE dimensions 500, 750, 1000, and 1125 μm, and observing that beyond 750 μm, material response does not vary more than 5%. With this trade-off, the computational time to generate calibration samples is reduced. To determine the values of the simulation parameters, the forward model needs to be run several times, which is computationally prohibitive. Therefore, an accurate and differentiable surrogate model is required. Current work considered two methods to build the surrogate models, HOPGD and INN. Using an FFT-based computation method, an offline database is prepared to build the surrogate model. The surrogate is used instead of the full field model to minimize J. Once a reasonable agreement between predicted and experimental stress values is obtained from Eqn. 12, the parameters are considered to be calibrated.

Higher-order Proper Generalized Decomposition (HOPGD)

The first surrogate model used in this work is based on the Higher-Order PGD (HOPGD) [43, 44]. The basic idea behind the HOPGD is the separation of variables. For a d-dimensional function $f(\mu_1, \mu_2, ..., \mu_d)$, expressing the quantity of interest as a function of parameters $\mu_i|_{i=1,d} \in \mathcal{D}_i$, the separation of variables results in the following form

$$\begin{aligned} f(\mu_1, \mu_2, ..., \mu_d) &\approx f^n(\mu_1, \mu_2, ..., \mu_d) \\ &= \sum_{m=1}^{n} F_1^m(\mu_1) F_2^m(\mu_2) \cdots F_d^m(\mu_d). \end{aligned} \tag{13}$$

Where f^n is an approximation of f, n is the rank of approximation, and m denotes the m^{th} mode. The superscripts n, m are counting indices, not exponents. The n-rank approximation, f^n, is given by the finite sum of products of the separated functions/modes: $F_i^m|_{i=1,d}$, which are *a priori* unknown and should be obtained either with a pre-computed offline database [31, 43, 44, 52–54] or by directly resorting to physical models [55–60]. The HOPGD relies on a pre-computed offline database. The database can be either from simulations or experiments. Once the database is obtained, the HOPGD can learn with data to compute the mode functions $F_i^m|_{i=1,d}$, which can reproduce (or extrapolate) the full parametric function f. Detailed implementation and a shared code can be found on the GitHub website [61].

In this work, the HOPGD is used to approximate the parametric stress–strain relationship for speeding up the calibration process, which can be written as

$$\sigma^{\text{HOPGD}} = \sigma^n(\epsilon, p_1, ..., p_6) = \sum_{m=1}^{n} F_\epsilon^m(\epsilon) F_1^m(p_1) \cdots F_d^m(p_6) \tag{14}$$

where $p_i = p_1, p_2, ..., p_6$ are the parameters $\boldsymbol{p} = \{\dot{\gamma}_0, \tau_0, m, H, h, \kappa\}$.

We remark here that the HOPGD model used in this work because it is relatively cheap to evaluate and optimize using the gradient descent algorithm. Moreover, the authors have used this method to participate and win an award in the NIST AM Bench 2022. The article aims to elaborate on that process and test whether the newly proposed INN algorithm can achieve a similar efficacy as HOPGD.

Interpolating Neural Network (INN)

Interpolating neural network (INN) is the second surrogate model development method used in this work. This is a novel network architecture that unifies machine learning, interpolation theory, and tensor decomposition (TD) [45]. Similar to HOPGD, INNs are based on the multiplicative decomposition of the input parameter domain, assuming the variation of each parameter can be captured with one-dimensional functions. However, INNs add more flexibility to the approximation and provide more general network architecture [45]. INN is the result of a series of developments of Hierarchical Deep Learning Neural Network (HiDeNN) [62], convolutional HiDeNN [63, 64], and HiDeNN-TD [65]. INN's learning capability considerably outperforms machine learning perceptrons (MLPs) when the dataset is sparse, making it a suitable candidate for calibrating material laws.

INN consists of three steps: 1) discretize each input parameter domain with a set of nodes, and represent it as a graph, 2) conduct message passing to construct interpolation functions on each graph node, and 3) optimize the nodal values (or the coordinates if needed) against a problem-specific

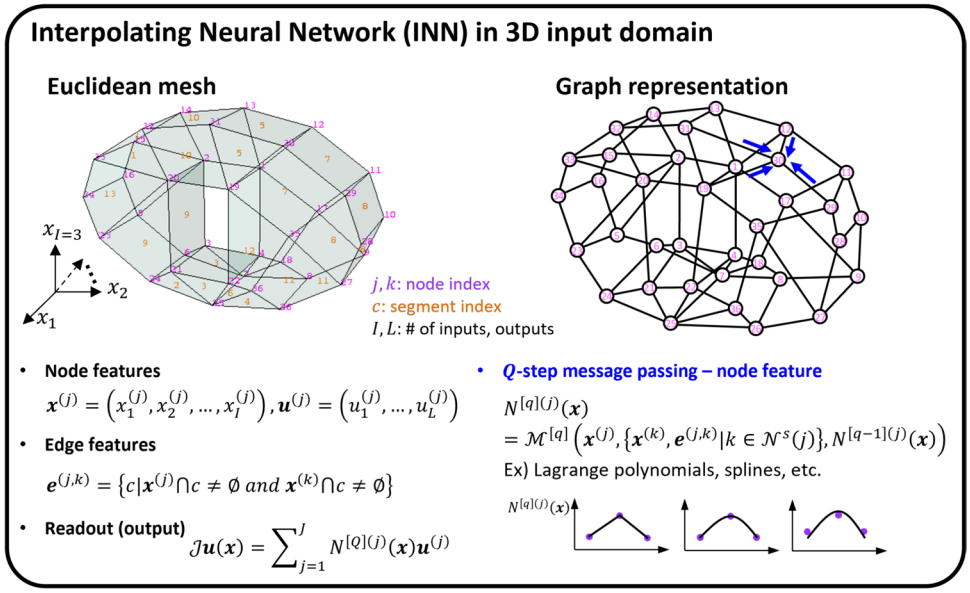

Fig. 9 Schematic of INN, redrawn from [45]

loss function. In this article, we use the mean squared error (MSE) loss function for supervised learning tasks.

Figure 9 illustrates an INN in the three-dimensional input domain. However, one can readily generalize to an arbitrary number of input–output dimensions. Given that an Euclidean three-dimensional space is discretized with non-overlapping segments, one can convert it into a graph where each graph node stores nodal coordinates $\boldsymbol{x}^{(j)}$ and nodal values $\boldsymbol{u}^{(j)}$ (the superscript (j) denotes the node index). The graph edge $\boldsymbol{e}^{(j,k)}$ stores indices of segments that are connected to the edge linking nodes j and k. The transformation of an Euclidean mesh into a graph is widely recognized in the literature [66–68].

Once the graph is constructed, the INN message passing generates interpolation functions on each graph node. A single-step message passing typically generates Lagrange polynomials. For instance, a step-1 message passing ($q = 1$) with single connectivity ($s = 1$, or hop) returns a linear interpolation function at each node:

$$N^{[q=1](j)}(\boldsymbol{x}) = \mathcal{M}^{q=1}(\boldsymbol{x}^{(j)}, \{\boldsymbol{x}^{(k)}, \boldsymbol{e}^{(j,k)} | k \in \mathcal{N}^{s=1}(j)\}), \tag{15}$$

where $\mathcal{N}^s(j)$ is the set of nodes surrounding the center node j with s connections. They are equivalent to the standard linear finite element shape functions.

One can systematically conduct Q-step message passing to build more adaptable and higher-order interpolation functions. Consider a step-2 message passing ($q = 2$) with $s = 2$ connectivity that builds nonlinear interpolation functions with quadratic ($p = 2$) polynomial reproducing order:

$$N^{[q=2](j)}(\boldsymbol{x}) = \mathcal{M}^{q=2}(\boldsymbol{x}^{(j)}, \{\boldsymbol{x}^{(k)}, \boldsymbol{e}^{(j,k)} | k \in \mathcal{N}^{s=2}(j)\}, N^{[q=1](j)}(\boldsymbol{x}), p = 2). \tag{16}$$

At this time, the interpolation function $N^{[q=2](j)}(\boldsymbol{x})$ is build upon its previous version $N^{[q=1](j)}(\boldsymbol{x})$ with enlarged neighbor domain $\mathcal{N}^{s=2}(j)$. The connectivity (or so-called patch size in [45, 63]) and polynomial order p are the key hyperparameters that define the interpolation functions. Details on this message passing operation can be found in [45].

When an input $x \in \mathbb{R}^I$ enters the network, each graph node computes the interpolation function value $N^{[Q](j)}(\boldsymbol{x})$ and multiplies it with its nodal value $\boldsymbol{u}^{(j)}$. The graph-level readout operation returns the network output: $\boldsymbol{u}(\boldsymbol{x}) = \sum_{j=1}^{J} N^{[Q](j)}(\boldsymbol{x}) \boldsymbol{u}^{(j)}$. Assuming that the nodal coordinates (the Euclidean mesh) are fixed, the only trainable variables are the nodal values, $\boldsymbol{u}^{(j)}$.

The computational complexity of the message passing scales exponentially with the input dimension I. One precise and mathematically well-developed reduced-order representation of such high-dimensional interpolation is the tensor decomposition (TD) [45, 65], where we transform the higher-order interpolation into one-dimensional interpolations. Interested readers may refer to [45] for more discussion.

This work uses INN as a supervised learning algorithm to construct a surrogate model. Suppose that there are K labeled experimental data for supervised learning: $(\boldsymbol{x}_k^*, \boldsymbol{u}_k^*)$, $k = 1, \cdots, K$; and $\boldsymbol{x}_k^* \in \mathbb{R}^I, \boldsymbol{u}_k^* \in \mathbb{R}^L$. The mean squared error (MSE) can be used for training:

$$\underset{\boldsymbol{U},\boldsymbol{X}}{\text{minimize}}\ loss(\boldsymbol{U}, \boldsymbol{X}) = \frac{1}{K} \sum_k (\boldsymbol{u}(\boldsymbol{x}_k^*) - \boldsymbol{u}_k^*)^2. \tag{17}$$

Here $\boldsymbol{U}$ and $\boldsymbol{X}$ are the sets of nodal values and coordinates, respectively. Both are trainable; however, it is more practical to fix the nodal coordinates $\boldsymbol{X}$ and train only for the nodal values $\boldsymbol{U}$ given that the input space is appropriately sampled. We followed this strategy with an adaptive sampling strategy (detailed in 3.5).

Once the forward surrogate model is trained, a calibration task is defined as an optimization problem:

$$\boldsymbol{x}^* = \underset{\boldsymbol{x}}{\operatorname{argmin}} \frac{1}{K} \sum_k (\boldsymbol{u}(\boldsymbol{x}) - \boldsymbol{u}_k^*)^2, \tag{18}$$

where we want to find out input parameters $\boldsymbol{x}^*$ that returns observed outputs $\boldsymbol{u}^*$. It is worth noting that the INN architecture is fully differentiable, like other neural network models, making it suitable for gradient-based optimization for the calibration task. The calibration framework can be written as:

$$\boldsymbol{x} = \{\epsilon, \boldsymbol{p}\}, \tag{19}$$

$$u(\boldsymbol{x}) = \sigma(\epsilon, \boldsymbol{p}), \tag{20}$$

$$J = \frac{1}{K} \sum_k (\sigma^{INN}(\boldsymbol{x}) - \sigma(\epsilon)_k^{Exp})^2, \tag{21}$$

where J is the calibration loss function, and $\boldsymbol{p}$ is the parameters to be calibrated. Sampling points in the strain are the same for each iteration of the forward pass. The sampling mismatch between the experiment and forward passes is compensated using linearly interpolated values of stress in the experimental set (as these are of higher fidelity) to match with computational sampling.

Sampling Strategy for Offline Database

An adaptive sampling strategy is followed in this work, which was first proposed by [44]. The technique is a sophisticated grid search method with adaptive updates. In general, for a parameter space $\mathcal{D}$ (usually large enough), the aim is to limit the required number of sampling points in the parameter identification procedure, thereby reducing the number of offline full-field simulations. The idea consists of incrementally enriching the database and using the optimization results to guide the sampling. This results in an adaptive sparse grid in $\mathcal{D}$ and is suitable even for a very high-dimensional space. This sampling method is applied for both HOPGD and INN surrogate construction. The main procedure is presented below with the help of Fig. 10.

- Start from the predefined space $\mathcal{D}$, sample the central axes of the space by adding two points at the extremities of each axis and one point at the center. In a two-dimensional space, this axis sampling results in a sparse grid of 5 points, as shown in Fig. 10a. Analogically, for an n-dimensional space, this number of points is $2n + 1$, which scales only linearly with n. This is advantageous for very high-dimensional cases. In the context of the current work, there are six calibration parameters.
- With the first level sampling, an initial surrogate model is constructed, and the first round of optimization is performed following Sect. 3.2. This optimization can be done with a gradient-based algorithm (e.g., Sequential Quadratic Programming (SQP)) with a multi-start strategy [44] (followed by HOPGD) or directly using a gradient descent algorithm for finding the global optimum (followed by INN) [45]. An example of this is indicated by a red point in Fig. 10a.
- Since the quality of the surrogate model depends on the amount of data (i.e., grid), most often only one level of sampling is not sufficient. Further refinement of the sampling space $\mathcal{D}$ is needed, and a repetitive check is performed to determine the quality of the surrogate. The idea is to go into a sub-level of the space, where the global optimum is located, then perform the axis sampling in that subspace, see, e.g., Fig. 10b. The global optimum will be changed with the updated surrogate model or stay close to the previous one. Depending on whether convergence is reached, the space can be further sampled in the same way or considered as the final one. In Fig. 10, convergence is assumed to be reached at level 3 for visual explanation.

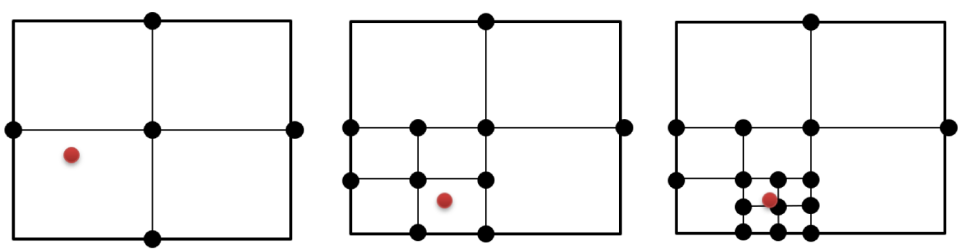

(a) Grid at level 1 (b) Grid at level 2 (c) Grid at level 3

Fig. 10 Adaptive sampling strategy for data generation. Black: sampling points (data), Red: current optimum. [44]

Optimization at each level has to be done with initial guesses of the parameters randomly chosen in the global space $\mathcal{D}$, even though the data enrichment is locally performed. For each local iteration, the acceptable error (mean squared error) level is considered to be 10^{-6} during training from sampled data.

Results

The results section presents a comparative analysis of the performance between HOPGD and INN surrogates. Later, the tensile response of IN 625 coupons is computed for different loading conditions and scanning strategies using both HOPGD- and INN-calibrated parameters. Based on the characterization data provided in [47], the computational model assumes that there are no porosity, residual stress, and foreign phase present in the RVE.

Comparison between Calibration Strategies

Figure 11 illustrates how the computational model performs with parameters calibrated by INN and HOPGD surrogates with respect to the calibration data. Computational time taken to run each CP simulation at each sampling point is 6.2-−9.9 h (depending on how many extra iterations it takes to converge during plastic deformation) with 128 nodes of AMD EPYC 7702 processor with 2 GHz speed. From the figure, it is apparent that, once calibrated, the computational model can have decent performance using either INN- or HOPGD-calibrated parameters. A closer inspection will tell the readers that INN calibration does match the onset of plasticity better than HOPGD parameters. However, the biggest difference comes in the amount of offline data required by these two methods. An accurate surrogate model with HOPGD required 68 sampling data points. On the other hand, INN required only 38 points, which is almost half the sampling data required by HOPGD. For a target test mean squared error (MSE) of 10^{-4}, the surrogate training took 68–69 s (depending on multiple runs) for both methods, with an R^2 score of 0.98 in an NVIDIA A6000 GPU machine. The INN and HOPGD surrogates take around 0.02 s to calibrate all the parameters with multiple forward passes, clearly indicating the speed-up.

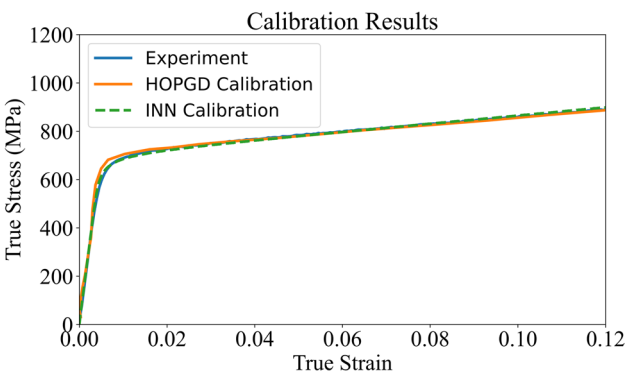

Fig. 11 A comparison of calibration performance between INN and HOPGD surrogate models

Both surrogates do a decent job considering that there are six parameters to be calibrated. The reason for INN outperforming HOPGD is the flexibility of the interpolation or approximation function in each parameter direction. INN can avail a higher order approximation by changing the hyperparameters and, therefore, can be more accurate with sparse data. This ability of INN makes the algorithm incredibly useful for complex parameterization problems such as this one. The method is also successfully applied to model the heat source parameters of the LPBF process [45]. A summary of the final calibrated parameters is presented in Table 2. The ranges considered are: τ_0: 280–310 MPa, $\dot{\gamma}_0$: 0.001-−0.003 s^{-1}, m: 50–100, H: 275–350 MPa, h: 0.0011-−0.0025 MPa, and κ: 0.4-−0.8. These ranges are selected heuristically from the authors' previous work [30, 31].

It is important to note from the table that the calibrated parameters with both methods are non-unique. It implies that, depending on the method or even the initial point of the gradient descent method, the final calibrated material parameters can be different. This non-uniqueness can affect the outcome of the computational model when sub-grain level information, such as fatigue crack initiation or local dislocation density, is needed. However, for a homogenization-type model, such as the one presented in this article, these differences do not significantly affect the features of the tensile stress–strain curve.

Table 2 Comparison of calibrated CP parameters by HOPGD and INN. $\dot{\gamma}_0, \tau_0, m, H, h$, and κ are calibrated

Material property	HOPGD	INN
C_{1111}	223,300 MPa	223300 MPa
C_{1122}	117800 MPa	117800 MPa
C_{2323}	156700 MPa	156700 MPa
$\dot{\gamma}_0$	0.0018 s^{-1}	0.0024 s^{-1}
m	70.0	80.4
τ_0	303.0 MPa	298.55 MPa
a_0	1.5 MPa	1.5 MPa
H	350.0 MPa	299.0 MPa
h	0.0012 MPa	0.00165 MPa
R	50.0 MPa	50.0 MPa
r	1.9425 MPa	1.9425 MPa
κ^*	0.58	0.508

*Internal variable of the material law

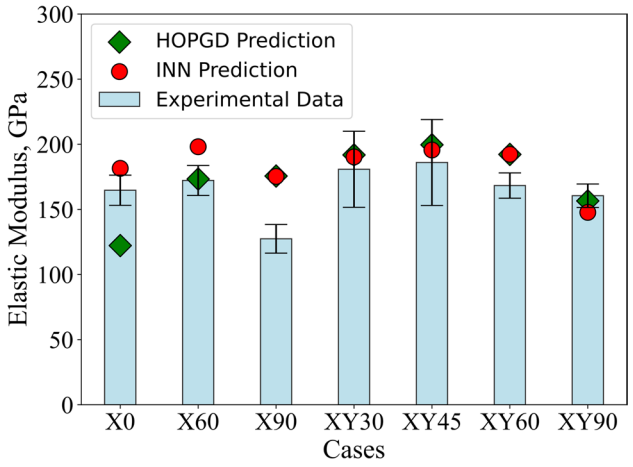

Fig. 12 Elastic modulus prediction along the loading direction for different scanning strategies with both INN and HOPGD. The bars on the experimental data show one standard deviation. In *Cases* axis, the letter indicates scan strategy, and the number denotes loading direction with respect to build direction

Effect of Manufacturing Conditions on Tensile Response

The predicted tensile responses include elastic modulus, yield strength, and true stress values at 5%, 10%, and 20% true strains. The first two quantities quantify the accuracy of predicting elastic properties, while the latter determines the accuracy of predicting plastic response. Figure 12 illustrates elastic modulus prediction for X and XY scanning strategies and at different loading orientations. From the figure, it is evident that both INN- and HOPGD-calibrated models perform well in predicting the elastic modulus. This is a consequence of both calibration methods using the same elastic constants. However, there are slight discrepancies due to variation in the onset of plastic deformation. In the X scanning strategy, the experimental data show that the elastic modulus increases from loading along the build direction to loading along an angle of 60^0, and then decreases to a lower value when loading is applied in the 90^0 angle. On the other hand, elastic modulus seems to reach a maximum when a tensile coupon is loaded at an angle of 45^0 with the build direction for XY scanning strategy. Elastic modulus gradually decreases with larger than 45^0 deviation from the build orientation. The reason can be attributed to the texture of the microstructure from both scanning strategies. While both scanning strategies produce columnar grains, it is more pronounced for X scanning. {001} and {101} poles are parallel to the build direction for the X-scan strategy. {001} poles start near the center of the scan tracks, and {101} appear near the edge of the scan track [47]. This change in grain morphology imparts variation in the tensile response. Figure 12 suggests that the computational model is able to capture this trend successfully whether the parameters are from HOPGD or INN. Predictions also suggest that, for most cases, INN-calibrated parameters are either doing slightly better or equally as good as the HOPGD parameters. However, for the X-scan strategy and along the build direction, INN parameters give markedly better prediction compared to HOPGD. Qualitatively, one additional remark can be made. Predictions for X-scanned samples are worse than XY-scanned samples. It is understandable as the calibration is done with XY-scanned sample and for loading along the build direction. Due to the noticeable difference in texture between X and XY scanning strategies, there is more error for X-scan prediction.

Figure 13 presents the 0.2% yield strength for two scanning strategies and along the different loading directions. In this case, the efficacy of INN-calibrated parameters for prediction is clearly more than the HOPGD-calibrated parameters. Apart from 90^0 angle from the build direction case, predictions with INN-calibrated parameters are better than the HOPGD parameters. For XY-scanned samples, both INN and HOPGD parameters give very good agreement with experiments. The onset of yield is controlled by the parameter τ_0 which is calibrated directly in this work. Therefore, close agreement of yield strength with experiment suggests successful calibration with only 38 data points for INN. Figure 13 suggests that XY scanning strategy results in coupons with larger yield strength compared to X-scanned samples. As mentioned before, the texture suggests a prominent presence of columnar grain structure in X-scanned samples. Though XY-scanned samples show qualitatively similar structure, the presence of columnar structure is less. This might contribute to the slight increase in yield strength at

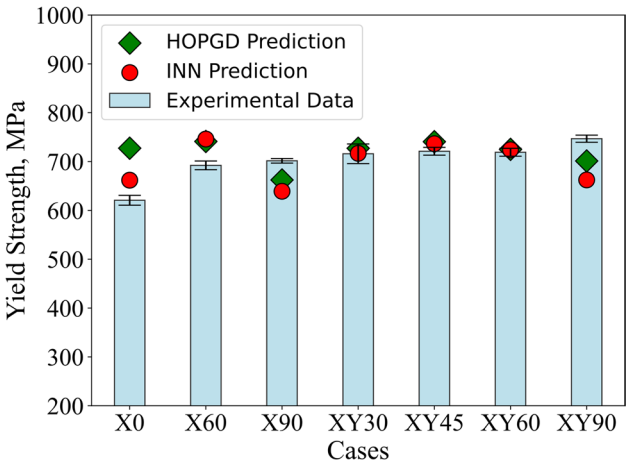

Fig. 13 Yield strength prediction along the loading direction for different scanning strategies with both INN and HOPGD. The bars on the experimental data show one standard deviation. In *Cases* axis, the letter indicates scan strategy, and the number denotes loading direction with respect to build direction

different loading directions. Another trend is that by increasing the angle between the loading direction with respect to the build direction, the yield strength of IN 625 coupon can be increased. Loading transversely seems to give the highest yield strength with either scan pattern. The computational model seemed to not do too well in case of 90^0 angle orientated sample. There is no apparent reason for this apart from a major discrepancy in the behavior of this case with respect to the calibration data.

Figures 14, 15 and 16 present the prediction of the plastic response of the IN 625 coupons for the manufacturing conditions considered. Figure 14 illustrates true stresses under 5% true strains for all the samples. Comparing values of stresses from Figs. 14 and 13, it is apparent that the material is already plastically deformed. Figure 14 shows that the prediction for INN is significantly better than HOPGD parameters. The only exception is again the case when the loading is applied at an angle of 90^0. Only in this case, the HOPGD prediction is closer to the experimental value. Although holistically, the prediction for this case is worse compared to other instances. For X scanning strategy, the coupon shows a strengthening as the loading is applied at a larger angle from the build orientation. The variation from experiments for X0 to X90 cases is also quite small, indicating indeed there is a strengthening. On the other hand, there is a sort of plateau in the stress response under 5% true strain at 30^0, 45^0, and 60^0 angles from the loading direction. Interestingly, for these three cases, INN prediction is very close to the experimental observation. The plateau effect is captured by the computational model successfully, indicating satisfactory calibration. Furthermore, the stresses are a little higher for XY-scanned samples compared to X-scanned samples.

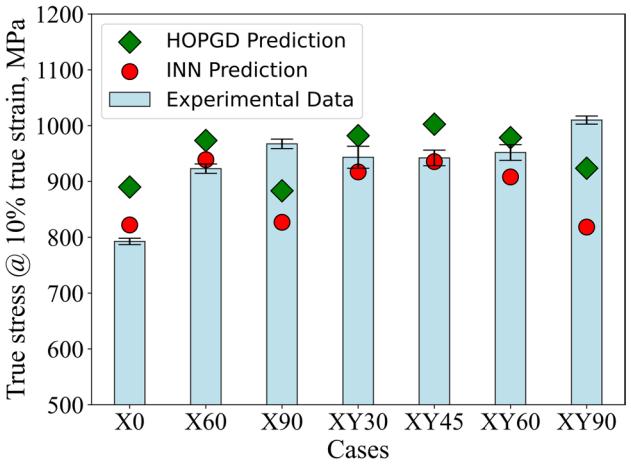

Fig. 15 True stress prediction at 10% true strain along the loading direction for different scanning strategies with both INN and HOPGD. The bars on experimental data show one standard deviation. In *Cases* axis, the letter indicates scan strategy, and the number denotes loading direction with respect to build direction

Figure 15 presents the true stress values under 10% true strain under different manufacturing conditions. It follows more or less the same pattern as discussed in Fig. 14. Again, the overall prediction accuracy of INN-calibrated model is comparable or better than the HOPGD-calibrated model. When loading is applied at an angle of 90^0, the models struggle to predict it from one calibration case. Although HOPGD-calibrated parameters seem to give a more accurate result compared to INN-calibrated parameters. Changing the angle from the build direction to the transverse direction clearly produced higher stress for X-scanned case. On the

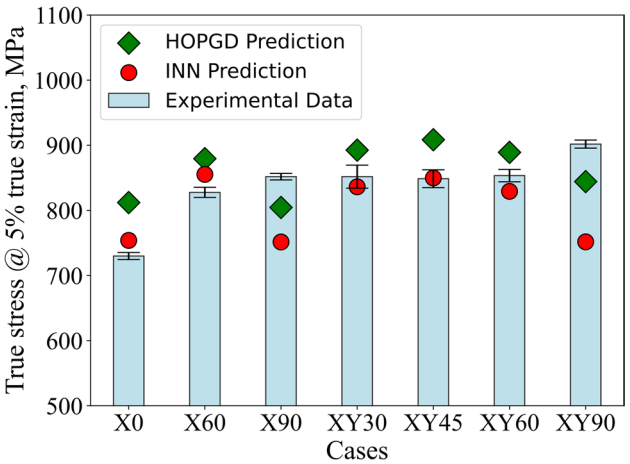

Fig. 14 True stress prediction at 5% true strain along the loading direction for different scanning strategies with both INN and HOPGD. The bars on the experimental data show one standard deviation. In *Cases* axis, the letter indicates scan strategy and the number denotes loading direction with respect to build direction

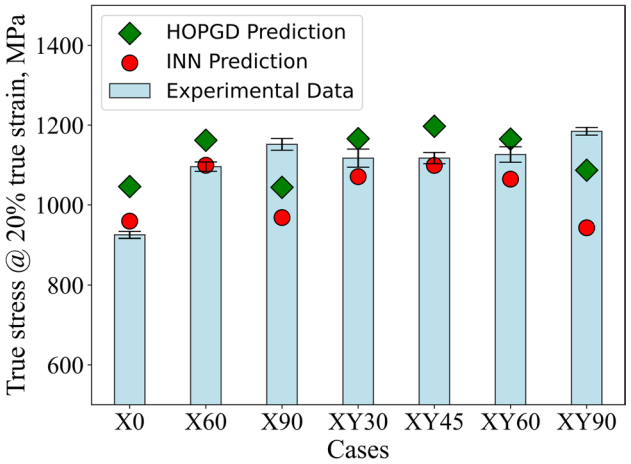

Fig. 16 True stress prediction at 20% true strain along the loading direction for different scanning strategies with both INN and HOPGD. The bars on the experimental data show one standard deviation. In *Cases* axis, the letter indicates scan strategy, and the number denotes loading direction with respect to build direction

other hand, a similar change did not bring much change in the resulting stress for XY-scanned samples. About 10% strain produces slightly higher stresses for XY60 and XY90 compared to X60 and X90. Figure 16 illustrates the same pattern as before. The model, whether calibrated by INN or HOPGD, does reasonably well to predict the values of stresses at different scan patterns and loading directions. The only exception is 90^0 loading direction. Generally, INN-calibrated parameters produce a more accurate prediction.

Conclusions

The article presents a systematic way to perform microstructure-based modeling of LPBF IN 625 alloy for different manufacturing conditions using limited calibration data. Current work introduces an adaptive method for sampling data generation to produce a surrogate of the expensive full-field computational model for calibration. A novel surrogate model development technique with an interpolation neural network (INN) is introduced, and its performance of calibration is analyzed with another widely used surrogate model, HOPGD. All the predictions are made using a crystal plasticity-based fast Fourier transform algorithm and validated using the NIST AM Benchmark 2022 dataset. The results suggest that combining adaptive sampling with INN can produce a highly accurate surrogate model that requires a relatively small set of offline computations. Moreover, such surrogates can be used alongside a gradient-based optimization algorithm, avoiding resorting to more expensive genetic methods. The computational model can successfully capture the effect of loading orientation with respect to the build direction and two different scanning strategies using representative volume element. Using two different scanning strategies imparts variation in the texture of the coupon. The calibrated parameters enabled the model to accurately capture the influence of the more columnar nature of X-scanned microstructures, which resulted in enhanced strength when loaded at an angle relative to the build orientation. For XY-scanned sample, a loading direction of 45^0 produces the maximum stiffness. The method presented here can be used for any alloy system produced by any advanced manufacturing techniques. It is to be noted that the adaptive sampling strategy discussed in this article does have a risk of reaching a local optimum instead of a global optimum after the first level of sampling. Hence, it is recommended that multiple runs of sampling be done to make sure that the optimization reaches the global minimum. The surrogate model development strategy can be extended to parametrize any physical law. The INN holds even greater promise to become a method that can be used as a trainer, solver, or inverse system designer. This potential will be discussed in a separate series of papers.

Editor's Video Summary The online version of this article (https://doi.org/10.1007/s40192-025-00425-2) contains an Editor's Video Summary, which is available to authorized users.

Acknowledgements S. Saha gratefully acknowledges the start-up fund provided by the Kevin T. Crofton Department of Aerospace and Ocean Engineering, Virginia Polytechnic Institute and State University. R. Batley acknowledges the Crofton Fellowship from the Kevin T. Crofton Department of Aerospace and Ocean Engineering, Virginia Polytechnic Institute and State University.

Data Availability The manuscript uses data available in the NIST Database. The HOPGD codes can be downloaded from https://yelu-git.github.io/hopgd/. The codes used for FFT simulation and optimization data are available in public repository Github. Any additional code required will be provided upon reasonable request.

References

1. Buchanan C, Gardner L (2019) Metal 3D printing in construction: a review of methods, research, applications, opportunities and challenges. Eng Struct 180:332–348
2. Armstrong M, Mehrabi H, Naveed N (2022) An overview of modern metal additive manufacturing technology. J Manuf Process 84:1001–1029
3. Jia Y, Naceur H, Saadlaoui Y, Dubar L, Bergheau J-M (2024) A comprehensive comparison of modeling strategies and simulation techniques applied in powder-based metallic additive manufacturing processes. J Manuf Process 110:1–29
4. King WE, Anderson AT, Ferencz RM, Hodge NE, Kamath C, Khairallah SA, Rubenchik AM (2015) Laser powder bed fusion additive manufacturing of metals; physics, computational, and materials challenges. Appl Phys Rev, 2(4)
5. Chowdhury S, Yadaiah N, Prakash C, Ramakrishna S, Dixit S, Gupta LR, Buddhi D (2022) Laser powder bed fusion: a state-of-the-art review of the technology, materials, properties & defects, and numerical modelling. J Market Res 20:2109–2172
6. Abd-Elaziem W, Elkatatny S, Abd-Elaziem A-E, Khedr M, Abd El-baky MA, Hassan MA, Abu-Okail M, Mohammed M, Järvenpää A, Allam T et al (2022) On the current research progress of metallic materials fabricated by laser powder bed fusion process: a review. J Market Res 20:681–707
7. Li X, Zhao C, Sun T, Tan W (2020) Revealing transient powder-gas interaction in laser powder bed fusion process through multi-physics modeling and high-speed synchrotron x-ray imaging. Addit Manuf 35:101362

8. Abdi M, Mosbah S, Ayadi M (2024) High fidelity multi-physics modeling of laser metal interaction and keyhole dynamics in powder bed fusion. Progress in Additive Manufacturing 1–18
9. Qin H, Fallah V, Dong Q, Brochu M, Daymond MR, Gallerneault M (2018) Solidification pattern, microstructure and texture development in laser powder bed fusion (LPBF) of Al10SiMg alloy. Mater Charact 145:29–38
10. Knapp GL, Raghavan N, Plotkowski A, Debroy T (2019) Experiments and simulations on solidification microstructure for inconel 718 in powder bed fusion electron beam additive manufacturing. Addit Manuf 25:511–521
11. Mohammadpour P, Yuan H, Phillion A (2022) Microstructure evolution of inconel 625 alloy during single-track laser powder bed fusion. Addit Manuf 55:102824
12. Arısoy YM, Criales LE, Özel T (2019) Modeling and simulation of thermal field and solidification in laser powder bed fusion of nickel alloy in625. Optics Laser Technol 109:278–292
13. Joshi S, Martukanitz RP, Nassar AR, Michaleris P (2023) Solidification during additive manufacturing. In: Additive manufacturing with metals: design. processes, materials, quality assurance, and applications. Springer, Cham, pp 427–480
14. Dixit S, Liu S, Murdoch HA, Smith PM (2023) Investigating build orientation-induced mechanical anisotropy in additive manufacturing 316l stainless steel. Mater Sci Eng, A 880:145308
15. Yang S, Zhang Y, Juan R, Li Z, Wu J, Akinwamide SO, Kuva J, Björkstrand RV, Lian J (2024) Effect of building orientation, thickness, and contouring on the microstructure and mechanical properties of alsi10mg via laser powder bed fusion. Mater Sci Eng A, 147685
16. Huang G, He G, Liu Y, Huang K (2024) Anisotropy of microstructure, mechanical properties and thermal expansion in invar 36 alloy fabricated via laser powder bed fusion. Addit Manuf 82:104025
17. Aiza I, Baldi C, Vega FM, Sebastiani S, Veronese NE, Yousefi M, Mosallanejad M, Maleki E, Guagliano M, Iuliano L et al (2024) Effects of build orientation and inclined features on physical, microstructural and mechanical properties of powder bed fusion additively manufactured metallic parts. Progress Mater Sci 10:101357
18. Watring DS, Benzing JT, Hrabe N, Spear AD (2020) Effects of laser-energy density and build orientation on the structure-property relationships in as-built inconel 718 manufactured by laser powder bed fusion. Addit Manuf 36:101425
19. Leicht A, Yu C-H, Luzin V, Klement U, Hryha E (2020) Effect of scan rotation on the microstructure development and mechanical properties of 316l parts produced by laser powder bed fusion. Mater Charact 163:110309
20. Yan W, Lian Y, Yu C, Kafka OL, Liu Z, Liu WK, Wagner GJ (2018) An integrated process-structure-property modeling framework for additive manufacturing. Comput Methods Appl Mech Eng 339:184–204
21. Yan W, Lin S, Kafka OL, Lian Y, Yu C, Liu Z, Yan J, Wolff S, Wu H, Ndip-Agbor E et al (2018) Data-driven multi-scale multi-physics models to derive process-structure-property relationships for additive manufacturing. Comput Mech 61(5):521–541
22. Mukherjee T, Wei H, De A, DebRoy T (2018) Heat and fluid flow in additive manufacturing-part ii: powder bed fusion of stainless steel, and titanium, nickel and aluminum base alloys. Comput Mater Sci 150:369–380
23. Gan Z, Lian Y, Lin SE, Jones KK, Liu WK, Wagner GJ (2019) Benchmark study of thermal behavior, surface topography, and dendritic microstructure in selective laser melting of inconel 625. Integr Mater Manuf Innov 8:178–193
24. Wang M, Han C, Jiang M, Trofimov V, Yang Y, Yang C, Feng Y, Yan M, Wei S, Wang D (2024) Molten pool behaviors and printability of tungsten anti-scattering grids with extremely thin wall thickness fabricated via laser powder bed fusion. Addit Manuf 94:104487
25. Leonor JP, Wagner GJ (2024) Go-melt: gpu-optimized multilevel execution of lpbf thermal simulations. Comput Methods Appl Mech Eng 426:116977
26. Trejos-Taborda J, Reyes-Osorio L, Garza C, Carmen Zambrano-Robledo P, Lopez-Botello O (2022) Finite element modeling of melt pool dynamics in laser powder bed fusion of 316l stainless steel. Int J Adv Manuf Technol 120(5):3947–3961
27. Lian Y, Lin S, Yan W, Liu WK, Wagner GJ (2018) A parallelized three-dimensional cellular automaton model for grain growth during additive manufacturing. Comput Mech 61:543–558
28. Sabau AS, Yuan L, Fattebert J-L, Turner JA (2023) An openmp gpu-offload implementation of a non-equilibrium solidification cellular automata model for additive manufacturing. Comput Phys Commun 284:108605
29. Rodgers TM, Madison JD, Tikare V (2017) Simulation of metal additive manufacturing microstructures using kinetic monte carlo. Comput Mater Sci 135:78–89
30. Saha S, Kafka OL, Lu Y, Yu C, Liu WK (2021) Macroscale property prediction for additively manufactured in625 from microstructure through advanced homogenization. Integr Mater Manuf Innov 10(3):360–372
31. Saha S, Kafka OL, Lu Y, Yu C, Liu WK (2021) Microscale structure to property prediction for additively manufactured in625 through advanced material model parameter identification. Integr Mater Manuf Innov 10(2):142–156
32. Roters F, Eisenlohr P, Hantcherli L, Tjahjanto DD, Bieler TR, Raabe D (2010) Overview of constitutive laws, kinematics, homogenization and multiscale methods in crystal plasticity finite-element modeling: theory, experiments, applications. Acta Mater 58(4):1152–1211
33. Wang Y, Zeng X, Sheng Y, Yang X, Wang F (2020) Multi-objective parameter identification and optimization for dislocation-dynamics-based constitutive modeling of ti-6al-4v alloy. J Alloy Compd 821:153460
34. Belytschko T, Liu WK, Moran B, Elkhodary K (2014) Nonlinear finite elements for continua and structures. John Wiley & Sons, Chichester
35. Savage DJ, Feng Z, Knezevic M (2021) Identification of crystal plasticity model parameters by multi-objective optimization integrating microstructural evolution and mechanical data. Comput Methods Appl Mech Eng 379:113747
36. Breumier S, Sao-Joao S, Villani A, Lévesque M, Kermouche G (2020) High strain rate micro-compression for crystal plasticity constitutive law parameters identification. Mater Des 193:108789
37. Veasna K, Feng Z, Zhang Q, Knezevic M (2023) Machine learning-based multi-objective optimization for efficient identification of crystal plasticity model parameters. Comput Methods Appl Mech Eng 403:115740
38. Dorward H, Knowles DM, Demir E, Mostafavi M, Peel MJ (2024) Calibration and surrogate model-based sensitivity analysis of crystal plasticity finite element models. Mater Des 247:113409
39. Frydrych K, Tomczak M, Papanikolaou S (2024) Crystal plasticity parameter optimization in cyclically deformed electrodeposited copper-a machine learning approach. Materials 17(14):3397
40. Lee J, Tasdemir B, Das S, Martin M, Knowles D, Mostafavi M (2024) Productive automation of calibration processes for crystal plasticity model parameters via reinforcement learning. Mater Des 248:113470
41. Kalidindi SR, Duvvuru HK, Knezevic M (2006) Spectral calibration of crystal plasticity models. Acta Mater 54(7):1795–1804
42. Sedighiani K, Diehl M, Traka K, Roters F, Sietsma J, Raabe D (2020) An efficient and robust approach to determine material

parameters of crystal plasticity constitutive laws from macro-scale stress-strain curves. Int J Plast 134:102779
43. Lu Y, Blal N, Gravouil A (2018) Adaptive sparse grid based HOPGD: toward a nonintrusive strategy for constructing space-time welding computational vademecum. Int J Numer Meth Eng 114(13):1438–1461
44. Lu Y, Blal N, Gravouil A (2019) Datadriven HOPGD based computational vademecum for welding parameter identification. Comput Mech 64(1):47–62
45. Park C, Saha S, Guo J, Xie X, Mojumder S, Bessa MA, Qian D, Chen W, Wagner GJ, Cao J, et al (2024) Engineering software 2.0 by interpolating neural networks: unifying training, solving, and calibration. arXiv preprint arXiv:2404.10296
46. Moulinec H, Suquet P (1998) A numerical method for computing the overall response of nonlinear composites with complex microstructure. Comput Methods Appl Mech Eng 157(1–2):69–94
47. Moser N, Benzing J, Kafka OL, Weaver J, Derimow N, Rentz R, Hrabe N (2024) Macroscale tensile challenge at different orientations (CHAL-AMB2022-04-MaTTO) and summary of predictions. Integr Mater Manuf Innov 13:155–174. https://doi.org/10.1007/s40192-023-00333-3
48. Groeber MA, Jackson MA (2014) Dream. 3d: a digital representation environment for the analysis of microstructure in 3d. Integr Mater Manuf Innov 3(1):56–72
49. Saha S (2024) Mechanistic computational intelligence (mci) from theory to practice: Opening pathways for a new generation of engineering software. PhD thesis, Northwestern University
50. Kabel M, Böhlke T, Schneider M (2014) Efficient fixed point and newton-krylov solvers for fft-based homogenization of elasticity at large deformations. Comput Mech 54(6):1497–1514
51. Wang Z, Stoica AD, Ma D, Beese AM (2016) Diffraction and single-crystal elastic constants of inconel 625 at room and elevated temperatures determined by neutron diffraction. Mater Sci Eng A 674:406–412
52. Lu Y, Blal N, Gravouil A (2018) Multi-parametric space-time computational vademecum for parametric studies: application to real time welding simulations. Finite Elem Anal Des 139:62–72
53. Blal N, Gravouil A (2019) Non-intrusive data learning based computational homogenization of materials with uncertainties. Comput Mech 64(3):807–828
54. Li Y, Mojumder S, Lu Y, Al Amin A, Guo J, Xie X, Chen W, Wagner GJ, Cao J, Liu WK (2024) Statistical parameterized physics-based machine learning digital shadow models for laser powder bed fusion process. Addit Manuf 87:104214
55. Néron D, Ladevèze P (2010) Proper generalized decomposition for multiscale and multiphysics problems. Archiv Comput Methods Eng 17(4):351–372
56. Ammar A, Mokdad B, Chinesta F, Keunings R (2006) A new family of solvers for some classes of multidimensional partial differential equations encountered in kinetic theory modeling of complex fluids. J Nonnewton Fluid Mech 139(3):153–176
57. Modesto D, Zlotnik S, Huerta A (2015) Proper generalized decomposition for parameterized helmholtz problems in heterogeneous and unbounded domains: application to harbor agitation. Comput Methods Appl Mech Eng 295:127–149
58. Ghnatios C, Masson F, Huerta A, Leygue A, Cueto E, Chinesta F (2012) Proper generalized decomposition based dynamic data-driven control of thermal processes. Comput Methods Appl Mech Eng 213:29–41
59. Lu Y, Li H, Saha S, Mojumder S, Al Amin A, Suarez D, Liu Y, Qian D, Kam Liu W (2021) Reduced order machine learning finite element methods: concept, implementation, and future applications. Comput Model Eng Sci 129(1)
60. Lu Y, Mojumder S, Guo J, Li Y, Liu WK (2024) Extended tensor decomposition model reduction methods: training, prediction, and design under uncertainty. Comput Methods Appl Mech Eng 418:116550
61. HOPGD-sHOPGD, https://yelu-git.github.io/hopgd
62. Saha S, Gan Z, Cheng L, Gao J, Kafka OL, Xie X, Li H, Tajdari M, Kim HA, Liu WK (2021) Hierarchical deep learning neural network (HiDeNN): an artificial intelligence (AI) framework for computational science and engineering. Comput Methods Appl Mech Eng 373:113452
63. Park C, Lu Y, Saha S, Xue T, Guo J, Mojumder S, Wagner GJ, Liu WK (2023) Convolution hierarchical deep-learning neural network (C-HiDeNN) with graphics processing unit (gpu) acceleration. Computational Mechanics
64. Lu Y, Li H, Zhang L, Park C, Mojumder S, Knapik S, Sang Z, Tang S, Apley DW, Wagner GJ et al (2023) Convolution hierarchical deep-learning neural networks (c-hidenn): finite elements, isogeometric analysis, tensor decomposition, and beyond. Comput Mech 72(2):333–362
65. Zhang L, Lu Y, Tang S, Liu WK (2022) Hidenn-td: reduced-order hierarchical deep learning neural networks. Comput Methods Appl Mech Eng 389:114414
66. Alet F, Jeewajee AK, Villalonga MB, Rodriguez A, Lozano-Perez T, Kaelbling L (2019) Graph element networks: adaptive, structured computation and memory. In: International Conference on Machine Learning, pp. 212–222. PMLR
67. Michelis MY, Katzschmann RK (2022) Physics-constrained unsupervised learning of partial differential equations using meshes. arXiv preprint arXiv:2203.16628
68. Gao H, Zahr MJ, Wang J-X (2022) Physics-informed graph neural galerkin networks: a unified framework for solving pde-governed forward and inverse problems. Comput Methods Appl Mech Eng 390:114502